1994ApJ...435..106N

THE ASTROPHYSICAL JOURNAL, 435:106–115, 1994 November 1
© 1994. The American Astronomical Society. All rights reserved. Printed in U.S.A.

X-RAY COLOR ANALYSIS OF THE SPECTRA OF ACTIVE GALACTIC NUCLEI

HAGAI NETZER
School of Physics and Astronomy and Wise Observatory, Beverly and Raymond Sackler Faculty of Exact Sciences,
Tel Aviv University, Tel Aviv 69978, Israel

AND

T. J. TURNER[1] AND IAN M. GEORGE[1]
Laboratory for High Energy Astrophysics, Code 668, NASA/Goddard Space Flight Center, Greenbelt, MD 20771

Received 1994 January 27; accepted 1994 May 3

ABSTRACT

The identification and detection of X-ray absorption and emission features depends on the resolution and the signal-to-noise ratio (S/N) of the observation, the understanding of the instrument response, and the Galactic line-of-sight absorption. Since many of the active galactic nucleus (AGN) data sets are limited in their S/N and full modeling of the physical conditions is rather complicated, we suggest a new analysis method based on "X-ray colors." The two sets of X-ray colors, defined for low (*ROSAT* PSPC) and medium (BBXRT and *ASCA* SIS) resolution experiments, are used to separate regions of different physical conditions in a two-dimensional color-color plane. They are similar but superior to previous methods using the X-ray "hardness ratio" in being able to reveal more of the physical properties of the source. We illustrate the use of such diagrams by studying a number of AGNs suspected of showing absorption features. A sample of 14 AGNs observed by the *ROSAT* PSPC is presented which includes several objects with suspected "warm absorbers" along the line-of-sight to the nucleus, several others exhibiting intrinsic continuum variations, and a number of control objects thought to be featureless. Our new observations show, for the first time, the color variation as a function of time for three of the Seyfert 1 sources: NGC 4051, Mrk 335, and Mrk 766. The variations suggest that in two sources we are witnessing real changes in continuum shape, while one (NGC 4051) is consistent with having a warm absorber. Four of the objects observed by BBXRT are reanalyzed using our X-ray colors. Out of these, we discuss in detail the case of NGC 4151 and show that the color-color analysis agrees very well with previous, detailed spectral fitting methods. In particular, we confirm that the observed BBXRT observation of this source is not consistent with the warm absorber explanation and must be interpreted as a combination of a variable hard component and another component. We explain the limitations in measuring low-energy emission features in *ASCA* SIS observations and present color-color diagrams which can be used as a powerful diagnostic tool in the analysis of data collected by this experiment.

Subject headings: galaxies: active — galaxies: nuclei — X-rays: galaxies

1. INTRODUCTION

There is mounting evidence that the X-ray spectra of active galactic nuclei (AGNs) are complex and cannot be described by simple power laws absorbed by neutral gas. Early observations (e.g., Reichert et al. 1985) showed evidence for large amounts of absorbing material in low-luminosity Seyferts galaxies. In some cases there was evidence that the absorbing material may be patchy, partially covering the X-ray source, or ionized, resulting in a reduced opacity in the 1 keV regime, compared to that expected from neutral ("cold") material (e.g., Reichert, Mushotzky, & Holt 1986, and references therein; Krolik & Kallman 1984; Yaqoob, Warwick, & Pounds 1989; Weaver et al. 1994). Recent *ROSAT* Position Sensitive Proportional Counter (PSPC) observations have now shown evidence for large absorbing columns intrinsic to some quasars showing the phenomenon is not limited to low-luminosity objects (Wilkes et al. 1992; Elvis et al. 1994; Laor et al., 1994).

The observed strength of the absorption features has been used to estimate the column density and level of ionization of the absorbing gas (the "warm absorber" case) or the covering factor and column density of the cold material (the "partial covering" case). A recent work by Netzer (1993) discusses the physical conditions in the ionized gas thought to give rise to the X-ray absorption and shows that emission and reflection by the highly ionized material is important in modifying the shape and the depth of the absorption troughs. Such effects are likely to show up in medium- and high-resolution X-ray spectra.

The identification and detection of X-ray absorption and emission features depends on the available X-ray resolution, the signal-to-noise ratio (S/N) of the specific observation, the understanding of the instrument response, and the Galactic line-of-sight absorption. Since many of the available data sets are limited in their S/N and full modeling of the physical conditions is rather complicated, we have devised a method of simplifying the analysis by the introduction of "X-ray colors." This approach, which is similar to the one used for many decades in optical and infrared astronomy, has proved to be very useful, and the present paper illustrates and discusses some of its more important assets. In § 2 we discuss various common AGN spectra and suggest the most suitable X-ray colors for several past and present experiments. In § 3 we apply our new technique to a sample of 14 AGNs observed by the *ROSAT* PSPC and to several Broad Band X-Ray Telescope (BBXRT) observations and show the time variability of the

---

[1] Also Universities Space Research Association.

© American Astronomical Society • Provided by the NASA Astrophysics Data System

new X-ray colors. In § 4 we summarize our results and suggest ways to analyze the forthcoming *ASCA* solid-state imaging spectrometers (SIS) data.

2. X-RAY SPECTRA AND X-RAY COLORS

2.1. *Theoretical X-Ray Spectra*

Previous investigations of expected X-ray spectra emphasized some aspects of absorption (Krolik & Kallman 1984; Halpern 1984), emission (e.g., Liedahl et al. 1990; Raymond 1994), and reflection (e.g., Lightman & White 1988). A more complete study has recently been published by Netzer (1993), and the present work closely follows that paper. For completeness, we give here a brief description of the more important assumptions and results.

We consider the physical conditions in material near a central source of ultraviolet and X-ray radiation. The gas is assumed to be clumped into clouds, of various sizes, that can be smaller or larger than the continuum source size. Photoionization is the only source for heating and excitation of the gas, and the observed X-ray spectrum depends upon the ionization parameter (defined as ionizing photon flux over $cN_{\rm H}$, where c is the speed of light and $N_{\rm H}$ the hydrogen number density), the gas density and composition, and the distribution of material around the center. X-ray absorption features can be weak or strong, depending on the column density, level of ionization, and fractional obscuration of the source. X-ray emission and reflection must be considered in all situations, and their relative strength depends on the ionization parameter and the covering fraction. For a given ionization parameter and column density, the strength of the emission and reflection components depends on the covering factor. For optically thin gas, maximum emission is for maximum covering, while for optically thick cases, the maximum occurs for a covering factor of 0.5. The situation investigated in the present work is the "large cloud" case discussed by Netzer (1993) in which a single cloud completely covers the central source but the overall covering factor, due to the entire cloud system, may be large or small. We do not discuss partial line-of-sight covering by ionized gas since this introduces an additional degree of freedom and since such cases are not going to show in absorption in most X-ray spectra, unless the covering factor by the small clouds is at least 0.9.

The numerical code used for calculating the ionization and emission properties of the gas is ION. The code utilizes a full, self-consistent, depth-dependent solution of the level of ionization of the gas and produces a list of all important emission and absorption features. Reflection by free electrons is calculated at all energies, given the distribution of the clouds (taken to be spherical in this work). A detailed description of the code, technical information, and illustrations are given in Netzer (1993).

In what follows we assume the same density (10^{10} cm^{-3}), composition (solar), and continuum shape as in Netzer (1993). This continuum shows a "blue bump," like many AGN spectra, and a smooth transition to the soft X-ray band. We have experimented with various X-ray power laws while maintaining an α_{ox} of about 1.3, typical of low-luminosity AGNs. The exact value of the X-ray power-law index Γ, defined here by $N_{h\nu} \propto h\nu^{-\Gamma}$, where $N_{h\nu}$ is the photon flux per unit energy, has little effect on the level of ionization but is of great importance when comparing with the spectral observations. For the high-energy part, we assume a sharp cutoff at 50 keV, again of little importance to the present study since the clouds are thin to this radiation. We have extended the range of the previous calculations by considering all column densities between 10^{21} and 10^{24} cm^{-2} and all ionization parameters over the range $10^{-0.8}$ (mostly neutral gas) to 10^2 (fully ionized gas). Figure 1 shows several examples of absorbed X-ray spectra with a column density of $10^{22.5}$ cm^{-2} and a range of ionization parameters. Two examples are shown: one for a pure absorption case (very small covering factor) and one for a case of maximum emission and reflection (covering factor of 0.5). Most realistic cases fall between these two extremes.

2.2. *Experimental Limitations*

The weakness of the majority of cosmic X-ray sources, combined with technical difficulties associated with grazing-incident mirrors of sufficient collecting area, have resulted in the vast majority of past and current X-ray spectrometers being nondispersive. Thus detector technology has centered around providing spectroscopic capability via the analysis of the amplified charge resulting from an individual incident photon which is collected by the detector readout electronics. Various electronic discriminators are then employed to quantize the charge in terms of a detected "count" (or event) in a given detector (spectral) "channel."

The atomic processes associated with the charge amplification and transport processes vary considerably between different instruments. However in almost all cases, the uncertainties associated with these stochastic processes give rise to instrumental responses (in terms of the number of counts registered as a function of detector channel) for a given mono-energetic photon input, which are (1) broad, (2) show significant departures from a Gaussian distribution, and (3) vary as a function of incident energy. The breadth of the instrumental responses give rise to the relatively poor spectral resolution of most X-ray experiments (compared to that possible with the use of dispersive optics). The result of all three effects is that it is not possible to perform a reliable unfolding of the instrumental response from an observed counts spectrum with typical S/N to obtain the incident spectrum. The skewness of the instrumental response of some devices is severe enough that there is a signficant probability that a high-energy incident photon will give rise to a count in the "low-energy" channel. On the most advanced current experiment, *ASCA* SIS, this occurs at the 1% level, but as we show below (§ 2.3.2), even this small effect has a significant influence on the ability to detect soft X-ray emission lines.

The most common approach to X-ray spectral analysis is that a two-dimensional (incident energy vs. detector channel) "redistribution matrix" is constructed from calibration measurements, each element of which gives the probability that an incident photon of that energy will result in an event in that channel of the detector readout electronics. Spectral analysis can then be performed via an iterative fitting process whereby a trial spectrum is folded through the matrix to determine the number of events predicted in each detector channel. This is then directly compared to the histogram of observed counts versus channel, the trial spectral model adjusted as necessary, folded through the matrix, and compared again until some statistical goodness-of-fit criteria is achieved. Such a method generally work very well for high-S/N data sets. However, for (the more common) low-S/N data, especially when the trial spectral models are complex and/or have a large number of variables, the method is less successful and is often unable to

1994ApJ...435..106N

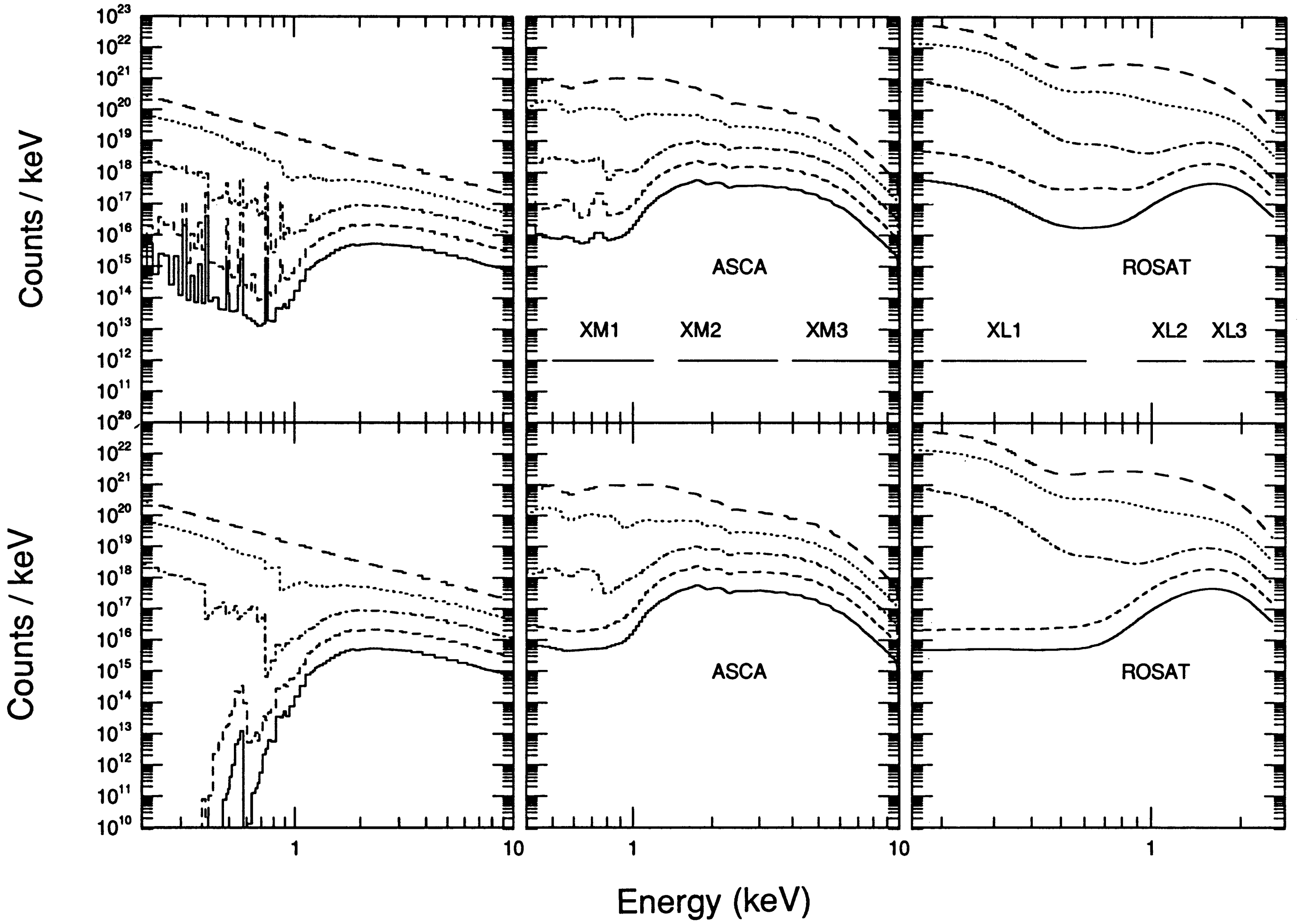

FIG. 1.—*Left panels*: Example predicted X-ray spectra for a system of clouds each with a column density of $10^{22.5}$ cm^{-2} and ionization parameter in the range $10^{-0.9}$ (*bottom curves*) to $10^{1.9}$ (*top curves*). Spectra corresponding to the general case (including absorption, emission, and reflection) are shown in the top panel and those with pure absorption are shown in the bottom panel. *Center and right panels*: Corresponding simulated spectra after convolution with the *ASCA* SIS and *ROSAT* PSPC detectors. Note in the case of the *ASCA* SIS, the difference between the simulated spectra for pure absorption and for the general case is small due to partial charge effects in the detector (see § 2.3.2).

usefully constrain parameter space. The detailed photoionization models described above are such models. Here we suggest a means of generalizing the results which takes into account the specific limitations, and capabilities, of various X-ray experiments.

2.3. *Color-Color Diagrams for ROSAT, ASCA, and BBXRT*

The idea of colors, extensively used in the analysis of optical and infrared observations, can be adopted in the X-ray range. This method, of comparing the boardband properties of various objects, suffers from the poor spectral resolution, but has the advantage of improved S/N and of uncovering the overall energy distribution of the source. It is also useful for grouping objects into classes and for detecting trends and regions in color-color diagrams. Here we apply this idea to several successful X-ray experiments.

We consider three experiments: the PSPC on board *ROSAT*, the SIS on board *ASCA*, and the BBXRT experiment flown as part of the *ASTRO-1* mission. We have used the available redistribution matrices for the three detectors (multiplied by the effective area of the corresponding telescope) to convert the calculated spectra to theoretical counts versus channel histograms. For illustration a number of spectra are shown in Figure 1 (*middle and right panels*). We have explored the entire energy range of each instrument and determined the best combination of three X-ray bands that separate objects according to their continuum shape, the absorbing column density, and the ionization parameter. Our best choice consists of three low-resolution bands, XL_1, XL_2, and XL_3, optimized for the *ROSAT* PSPC, and three medium-resolution bands, XM_1, XM_2, and XM_3, optimized for the *ACSA* SIS and BBXRT instruments. The channel and nominal energy ranges of the different colors are listed in Table 1, and some of the considerations in making this choice, as well as explanations of required correction factors, are given below. Our aim is to make the analysis as useful and as simple as possible; thus we calculate the colors from *detector count rates* (after making the necessary vignetting corrections) rather than from derived energy or photon fluxes.

2.3.1. *The ROSAT PSPC Colors*

Two PSPCs are provided as part of the focal plane assembly of the main X-Ray Telescope (XRT) on board *ROSAT* (Trümper 1983). These are essentially identical multiwire pro-

© American Astronomical Society • Provided by the NASA Astrophysics Data System

1994ApJ...435..106N

TABLE 1

DEFINITION OF X-RAY COLORS

Color	Range (keV)
ROSAT:	
XL_1	0.2–0.6
XL_2	0.9–1.3
XL_3	1.5–2.2
ASCA and BBXRT:	
XM_1	0.5–1.2
XM_2	1.5–3.5
XM_3	4.0–10.0

portional counters with a cathode strip readout for positional determination, providing a spectral resolution $\Delta E/E \simeq 0.43\,(E/0.93)^{-0.5}$ (FWHM), where E is the photon energy in keV, over a bandpass of ~0.1–2.4 keV (Pfeffermann et al. 1986). The spatial resolution over the full bandpass is ~25″ (FWHM) on-axis (Hasinger et al. 1992), increasing to ~44″ (FWHM) 11′ off-axis (Hasinger et al. 1993).

In order to calculate the theoretical count rate histograms we have used the convolution of the current detector redistribution matrix and XRT effective area curves for PSPC-B (referred to by the NASA/GSFC *ROSAT* Guest Observer Facility as pspcb_93jan12.rmf). However, neither the use of detector efficiencies corresponding to PSPC-C, nor the residual uncertainties in the above matrix, significantly affect the results presented here. Below we do not consider the case when the moveable boron filter is inserted into the light path.

The XL_1 band (0.2–0.6 keV) is designed to sample the range most important for distinguishing between pure absorption models and those with emission and reflection (Fig. 1, *left panels*). We avoided using data below 0.2 keV for three reasons: (1) the detector calibration uncertainties increase below 0.2 keV, (2) the absorption correction (for Galactic line-of-sight material) increases rapidly as we extend the bandpass to softer energies (see below), and (3) the lower discriminator for valid events changes as the detector gain changes, as the gas flow rate for the PSPC has been decreased for AO4, then the lower limit for valid events is likely to change again. Our choice of 0.2 keV should allow the figures in this paper to be used for all PSPC data, even A04 data taken after the gas flow rate change.

The XL_2 band (0.9–1.3 keV) is where we expect to observe a depletion of counts due to the warm absorber, given the range of parameter space thought to be applicable to AGNs. Thus, the ratio of counts accumulated in this band and the others is a key indicator of the amount of absorbing material present that is intrinsic to the AGN.

The third *ROSAT* band, XL_3 (1.5–2.2 keV), is specified by the requirement of obtaining a constraint on the continuum form above the spectral modifications due to absorption. It is extended as far as possible to soft energies to increase the S/N, while being distinct from the regime in which we expect the signature of absorption (XL_2). The XL_3 band is limited at the high end by the falloff in effective area and the uncertainties in the instrument calibration above 2 keV (due to factors such as uncertainties in the optical constants of gold).

We have experimented with different ranges for the respective bands, including cases of overlap and complete coverage of the *ROSAT* range. We found that the above choice is preferred over all others and the somewhat increased S/N in complete overlap cases causes undesired ambiguities in the color-color diagrams to be discussed below.

Prior to the comparison of observed data sets with the model predictions, one must correct the raw data for Galactic absorption, that is, an additional cold component, not included in the modeling. The following expression gives the multiplication factor to be applied to the measured XL_1 band, with an accuracy of about 10%, for absorbed power laws and for galactic columns of $1\text{–}10 \times 10^{20}\ \mathrm{cm}^{-2}$:

$$\mathrm{COR}_{XL_1} = \begin{cases} \exp(0.7C_{20}) & \text{if } C_{20} < 1.3\,, \\ 1.45C_{20} + aC_{20}^2 & \text{otherwise}\,, \end{cases} \tag{1}$$

where C_{20} is the neutral hydrogen column density in units of $10^{20}\ \mathrm{cm}^{-2}$ and the constant a depends on the photon index, Γ, and is given in the range $1.7 < \Gamma < 3$ by

$$a = 0.05 + 0.2(\Gamma - 2)\,. \tag{2}$$

For the XL_2 band the correction multiplication factor is much smaller and is given, to a good accuracy, by

$$\mathrm{COR}_{XL_2} = \exp(0.023C_{20})\,. \tag{3}$$

No correction is required for the XL_3 band for galactic columns of less than $2 \times 10^{21}\ \mathrm{cm}^{-2}$.

The color-color diagrams for *ROSAT* ($\log(XL_1/XL_2)$ versus $\log(XL_3/XL_2)$) are shown in Figure 2. The curves represent different column density ionized absorbers and are marked by the appropriate value. A model of photon spectral index of slope 1.9 was used for this case. For each of the chosen columns, a grid of models, covering the entire specified range of ionization parameter, was calculated. The low ionization parameter case is on the left-hand side of most of the curves. As the ionization parameter increases, the gas becomes increasingly transparent until the "bare continuum" is seen through. The bare continuum points of all column densities thus show as a single point on the color-color diagram, which is where all lines converge. For comparison, we also show three other curves: (1) a line corresponding to unabsorbed power laws of different slopes (the bare-continuum point joins the graph at $\Gamma = 1.9$), (2) a broken power-law curve where the 1–50 keV slope is 1.9 and the 0.2–1 keV continuum is steeper, by different amounts, and (3) a collection of optically thin, hot plasma models, for various electron temperatures. (Note that the most significant effect on the color-color tracks of changing the spectral index of the underlying power law is to move the tracks in such a way that bare-continuum point sits on the "pl" line at the appropriate place. The change in shape of the various curves is of lesser importance.)

The two panels of Figure 2 demonstrate the different assumptions about the covering factor of the ionized gas. The case shown in the bottom panel is that for a very small covering factor, approaching a pure absorption case. The top panel includes the maximum amount of emission and reflection, with a covering factor of 0.5. The difference between the two is large, due to the much larger range of colors expected in the pure absorption case (note the different limits on the axes of the two panels). The reason is the much reduced count rate in band XL_1, and to a lesser extent in band XL_2, in cases of large absorbing columns. The range is much more restricted for the general case, where reflection and emission contribute a lot to those bands, even when the original continuum is completely

© American Astronomical Society • Provided by the NASA Astrophysics Data System

1994ApJ...435..106N

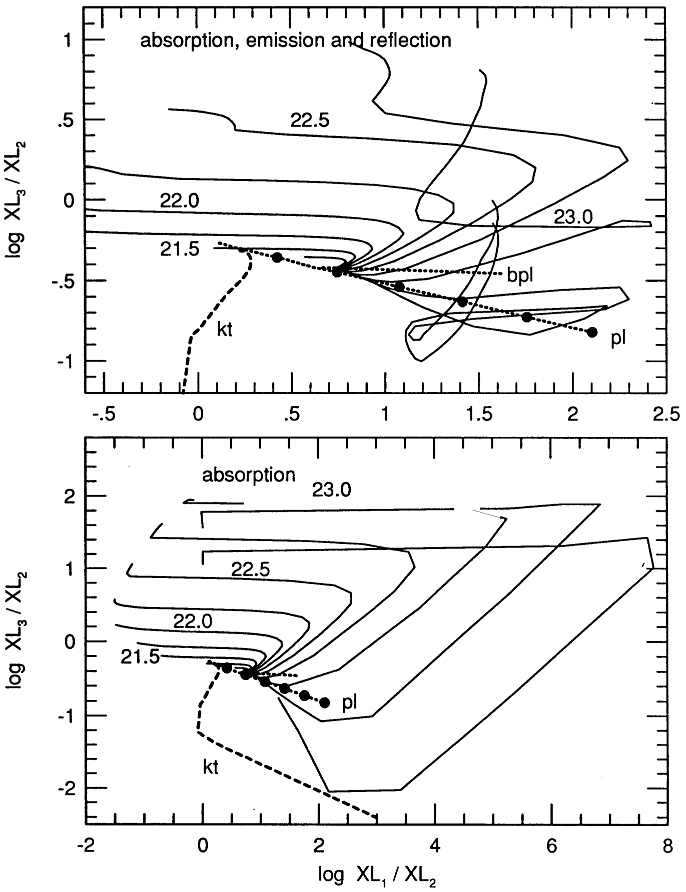

FIG. 2.—Color-color diagram for the *ROSAT* PSPC. *Top panel*: Model predictions for cases with absorption, emission, and reflection. Each line corresponds to a certain absorbing column (marked with the value of log (column)) and the ionization parameter increases from left to right, along the lines. All curves converge to one point, representing a very high ionization parameter and, thus, an essentially transparent cloud transmitting a "bare" continuum. The X-ray continuum photon slope is 1.9. The dotted line marked "pl" represent power laws with different slopes (increasing from left to right and marked at intervals of $\Delta\Gamma = 0.5$), and the one marked with "bpl" broken power-law continua where the 1–50 keV continuum photon index is 1.9 and the soft continuum is steeper. The effect on the color-color tracks of changing the spectral index of the underlying power law is to move the tracks in the color-color plane such that bare-continuum point sits on the "pl" line at the appropriate place. The dashed line marked with "kt" is a collection of hot, optically thin plasma models of different temperatures (increasing from bottom to top, meeting the "pl" line at $kT \sim 80$ keV). *Bottom panel*: Same as above, but for a pure absorption case. Note the much larger range resulting from the large reduction in the XL_1 count rate of the pure absorption models with large columns and low ionization parameter.

obscured. Those effects can be understood by investigating the spectral behavior shown in Figure 1 (*left panels*).

As can be seen from the upper panel of Figure 2, in the general case (emission and reflection included) the complexity of the spectrum results in complex tracks in the color-color plane for models above some critical column density. In this regime the tracks are no longer well separated, and dual, and even triple, points are possible. In the type of models investigated here, this occurs for column densities greater than approximately $10^{22.75}$ cm^{-2}. We can thus conclude that a color combination falling in the region to the bottom and the right of the bare-continuum point gives little information about the column density and the ionization parameter of the absorbing gas.

2.3.2. *The BBXRT and ASCA SIS Colors*

The BBXRT was flown with the *ASTRO-1* ultraviolet instruments as part of the Columbia (STS 35) shuttle payload on a 9 day mission over 1990 December 2–10. The instrument consisted of two co-aligned, nested-foil XRTs (Serlemitsos et al. 1992). The BBXRT mirrors were among the first allowing reflection of X-ray photons above ~4 keV and in many ways were the predecessors to those used for the *ASCA* XRTs (below). The focal plane detectors consisted for cooled, lithium-drifted silicon solid-state spectrometers providing an effective bandpass of ~0.3–12 keV.

The effective area of each of the BBXRT telescopes was 160 cm^2 at 1.5 keV and 75 cm^2 at 7 keV, with energy resolution of ~90 eV at 1 keV and ~150 eV at 6 keV. The detector background was very low, contributing ~0.02 counts s^{-1} in the central pixel, and 0.1 counts s^{-1} in each outer pixel. BBXRT provided negligible spatial resolution, with each detector segmented into only 5 pixels: with the central pixel having a 4′ diameter field of view and a total diameter of 17′. The theoretical count rate histograms calculated here were derived using the convolution of the redistribution matrix for detector A (pixel 0) and the corresponding XRT effective area curve. However, our results are equally valid for detector B (pixel 0).

An SIS is provided as the focal plane detector under two of the four co-aligned, nested-foil XRTs on board *ASCA* (Tanaka et al. 1994). Each SIS consists of four essentially identical front-illuminated, frame-transfer CCDs, providing a spectral resolution of $\Delta E/E \simeq 9\ [(N/1000E)^2 + 0.12/3.7 \times 10^3 E]0.5$ (FWHM), where E is the photon energy in keV, over a bandpass of ~0.4–12 keV, and N is the RMS readout noise of the preamplifier (with $N^2 \sim 20$ at 6 keV). In order to calculate the theoretical count rate histograms we have used a preflight convolution of the detector redistribution matrix and XRT effective area curves for an SIS (referred to by the NASA/GSFC *ASCA* Guest Observer Facility as sis_small.rmf).

Since the useful energy range of both the *ASCA* SIS and BBXRT experiments is ~0.4–10 keV, the ideal combination of X-ray bands would be one which is capable of separating the very low energy range ($E < 0.8$ keV) and thus enabling pure absorption cases (Fig. 1, *bottom left panel*) to be distinguished from those with reflection and emission (Fig. 1, *top left panel*). Unfortunately, this cannot be done with either solid-state detector, due to partial charge effects, as is demonstrated in Figure 3. This diagram shows an enlargement of two theoretical curves from Figure 1, one for pure absorption and the other for all the components. As is evident from the top two curves, which show the expected *ASCA* count rates for the theoretical models, the difference in the broadband integrated count rate between the two cases is small. The reason is mostly due to partial charge collection and charge trapping when a fraction of the charge created by incident photons diffuses into the "dead layer" of the CCD or is lost by other means (e.g., escaping Auger electrons and photoelectrons) rather than being registered by the anode. This is a well known, but complex feature of Si(Li) detectors which depends upon the detailed design of the CCD (e.g., see Weaver et al. 1994, and references therein). Thus, while very high S/N observations may detect such features, the change in count rate over a large band is small.

The best alternative is therefore to have a single band, XM_1, covering the region of strong absorption, a second band, XM_2, measuring the flux on the rising side of strong absorption features, which is sensitive to the absorbing column and the abun-

© American Astronomical Society • Provided by the NASA Astrophysics Data System

1994ApJ...435..106N

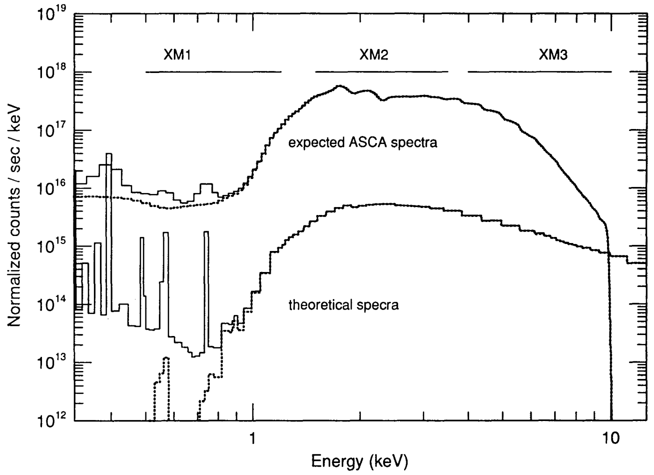

FIG. 3.—Comparison between theoretical models and the *ASCA* count rates. The theoretical spectra show large differences between pure absorption and the general case, over the XM_1 range (0.5–1.2 keV). However, the resulting *ASCA* SIS count rates are almost identical (*two upper curves*) because of partial charge in the solid-state detector. These two curves cannot be distinguished by any broadband analysis. However, good S/N data may show the predicted emission lines (*top curve*, at around 0.6 and 0.8 keV) that are not present in the pure absorption case.

dance of the heavy elements, and a third color, XM_3, at high energies, to establish a flux level which is independent of absorption of strong absorption features.

As in the case of *ROSAT*, some correction for Galactic absorption is required for the XM_1 band. The measured counts over the band should be multiplied by

$$\mathrm{COR}_{XM_1} = \exp(aC_{20}) , \tag{4}$$

where

$$a \simeq 0.0217 + 0.0145(\Gamma - 2) . \tag{5}$$

The multiplication correction factor for the XM_2 band is very small and can be approximated by

$$\mathrm{COR}_{XM_2} = \exp(4 \times 10^{-3} C_{20}) . \tag{6}$$

Finally, we have subdivided the XM_3 range, which is not likely to be affected by any absorption, into two, to facilitate an easy measure of the photon index Γ. Define XM_3a as the *ASCA* SIS observed counts between 4 and 6 keV, and XM_3b as the counts between 6 and 10 keV; we get

$$\Gamma \simeq \frac{\log(XM_{3a}/XM_{3b}) - 0.374}{0.159} . \tag{7}$$

The color-color diagrams for *ASCA* ($\log(XM_1/XM_2)$ vs. $\log(XM_3/XM_2)$) are shown in Figure 4. The BBXRT diagrams are very similar, covering an almost identical range in X-ray colors; they are not shown (to avoid making the figure unnecessarily complex). Here again we show curves corresponding to power-law continua with different slopes and optically thin plasma models of different temperatures.

The advantage of a higher resolution, larger energy range experiment are clearly seen on the diagrams. In particular, the curves corresponding to different columns are well separated and the identification of a unique pair of column density and ionization parameter, by colors, is valid up to the very large column density of $10^{23.5}$ cm^{-2}. The region to the bottom and the left of the power law curve is occupied by concave X-ray spectra, and the one to the right of it by those with a soft excess. All other locations, above the broken power-law curve, correspond to absorbed X-ray spectra, with low-energy slope as given here.

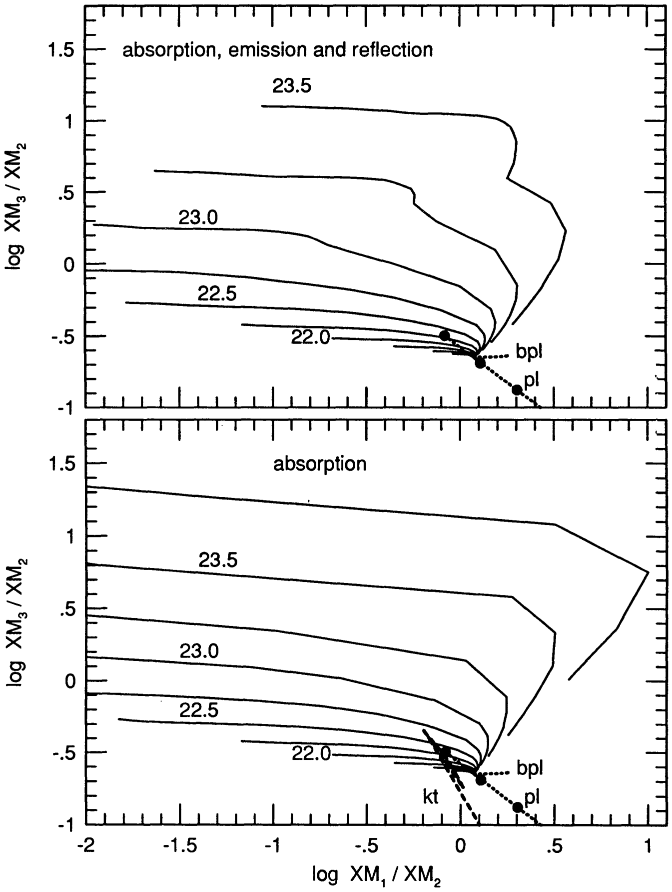

FIG. 4.—Same as Fig. 2, for *ASCA* SIS. In this case, the difference between pure absorption and full model is much smaller. This is due to the partial charge effect explained in the text and demonstrated in Fig. 4.

3. COMPARISON WITH OBSERVATIONS

3.1. *The ROSAT Sample*

3.1.1. *Observations*

Fourteen *ROSAT* PSPC observations are presented here. Some of these have been previously described in other papers, Mrk 335, NGC 7469, MCG−2-58-22, ESO 198−G24, ESO 141−G55, and Mrk 509 in Turner, George, & Mushotzky (1993b); Mrk 372, NGC 1365, and Mrk 3 in Turner, Urry, & Mushotzky (1993d), and NGC 3783 in Turner et al. (1993c). Additional data include the archival observations of NGC 4151 and NGC 4051 (Pounds et al. 1994) a BL Lac object, H1426+428 (included for comparison), an extended observation of Mrk 766 and a serendipitous observation of NGC 3227. Table 2 shows the observation log for all of the sources.

The PSPC data were processed using the Standard Analysis Software System to apply the aspect solution, convert the observed pulse-height analyzer channels to a standard pulse-invariant (PI) scale, and to select "good time intervals" (i.e. those data collected during acceptable satellite and detector operating parameters).

© American Astronomical Society • Provided by the NASA Astrophysics Data System

1994ApJ...435..106N

TABLE 2

ROSAT PSPC SOURCE LIST

Source Name	Observation Date	Integration Time[a] ($\times 10^3$ s)	Observed Count Rate[b] (counts s^{-1})	Observed Flux[c] ($\times 10^{-11}$ ergs s^{-1})	Off-Axis Angle[d]
Mrk 335	1991 Jun 29–30	2.46	1.747 ± 0.008	2.4	40′
ESO 198−G24	1991 Dec 22	4.31	2.98 ± 0.003	3.4	0
Mrk 372	1992 Aug 15–22	12.68	0.276 ± 0.005	0.3	0
NGC 1365[e]	1992 Aug 22–23 1993 Feb 05–10	8.79	0.117 ± 0.008	1.0	0
Mrk 3[e]	1991 Mar 13–28 1992 Mar 13–Apr 06	13.22	0.058 ± 0.003	0.6	0
NGC 3227	1992 May 08–09	26.52	0.254 ± 0.005	0.7	55
NGC 3783	1992 Jul 23	2.67	1.07 ± 0.02	1.3	12
NGC 4051	1991 Nov 16	28.73	1.518 ± 0.008	1.0	0
NGC 4151	1991 May 31–Jun 01	38.13	0.559 ± 0.004	0.5	0
Mrk 766	1992 Dec 21–23	19.87	3.24 ± 0.01	3.0	13
H1426+428	1991 Jan 24	9.59	3.85 ± 0.02	3.1	0
ESO 141−G55	1991 Mar 14–15	5.02	1.94 ± 0.02	2.4	0
Mrk 509	1991 May 10	1.96	3.18 ± 0.04	3.3	0
NGC 7469	1991 Nov 19	4.25	2.93 ± 0.03	3.4	0
MCG−2-58-22	1991 Nov 21	3.53	3.82 ± 0.03	3.9	0

[a] Good time intervals only.

[b] PSPC PI channels 12–200.

[c] 0.1–2.0 keV, uncorrected for Galactic line-of-sight absorption.

[d] Accurate to ±1′.

[e] Summed exposure and mean count rates and fluxes over the two epochs.

3.1.2. *Light-Curve Analysis*

Light curves were extracted using an extraction cell appropriate to the offset angle at which each target was observed (Hasinger et al. 1993). A source-free region at a similar offset angle was chosen as the background region in each case. Figure 5 shows the background-subtracted light curves, in the XL_1 band, of the longer observations in our sample: Mrk 335, NGC 3227, NGC 4051, and Mrk 766. The data were integrated such that one data point is shown per observation interval (typically 2000 s). In the case of 335, which was observed during the long pointing phase of *ROSAT*, the data gaps are even and of about the same duration as the data trains. In the NGC 3227, NGC 4051, and Mrk 766 observations, there are some longer gaps where the observations were broken up in time. The observation of NGC 4151 showed little source variability ($\lesssim 10\%$) across the observation and nine other observations were too short for a variability study.

The top panels of Figure 5 show the corrected (for Galactic absorption and vignetting) XL_1/XL_2 ratios for the four galaxies. In two cases, Mrk 766 and NGC 4051, there is a clear inverse correlation between the source luminosity and XL_1/XL_2. This is also the case for Mrk 335 between time 2×10^4 and 8×10^4 s, but the first two points in the light curve of the object deviate from this simple relation. Time lag between the response of the two bands, due to a possible delay of the emitting material, is one possible explanation, but the data are sufficient to evaluate this idea on a more quantitative base. The data for the fourth variable object, NGC 3227, are too noisy to detect a trend.

3.1.3. *Color-Color Diagrams*

The locations of the objects in our *ROSAT* sample on the color-color diagram are shown in Figure 6. This diagram is plotted for the case of an unabsorbed power-law continuum of photon index 2.5, the mean slope in our sample. The objects are separated into groups; in the top panel are those with known color changes (the three variable Seyfert 1s shown in Fig. 5), and in the bottom panel are those with a single point

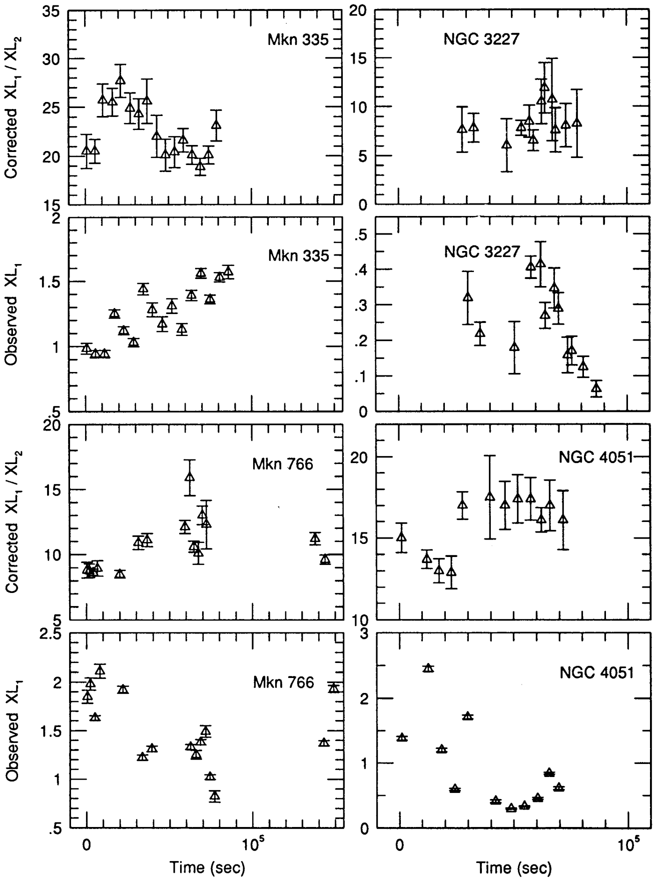

FIG. 5.—Observed XL_1 count rate and XL_1/XL_2 vs. time (latter corrected for Galactic absorption and vignetting) from *ROSAT* PSPC observations for the four variable Seyfert galaxies in our sample. Three sources, Mrk 335, Mrk 766, and NGC 4051, exhibit clear color changes, with XL_1/XL_2 anticorrelated with XL_1 for Mrk 766 and NGC 4051 and for the majority of points in the case of Mrk 335.

1994ApJ...435..106N

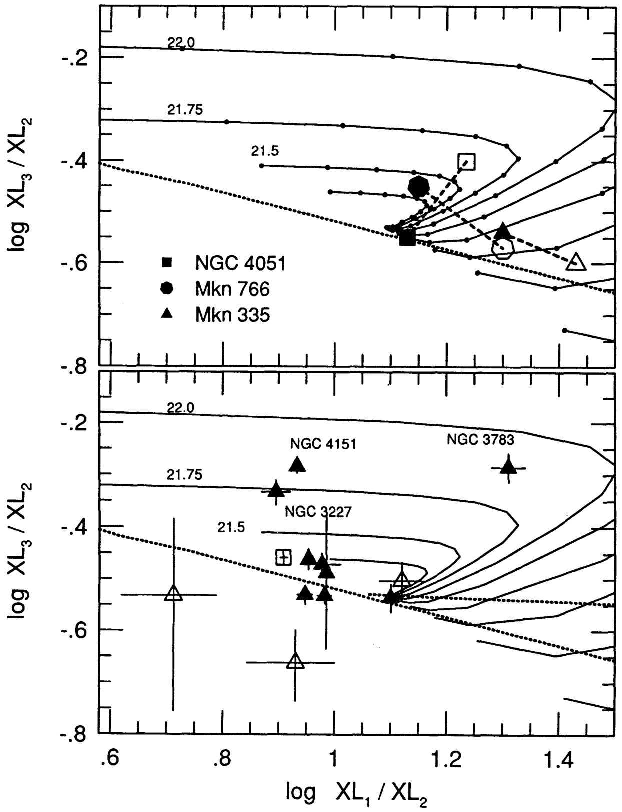

FIG. 6.—*ROSAT* color-color diagram for a case of X-ray continuum photon slope of 2.5 and full (emission and reflection included) model. The location of all objects is shown with names indicated for those suspected of warm absorber absorption. *Top panel*: The three variable Seyfert 1 galaxies from Fig. 5. Full and open symbols represent bright and faint continuum phases, respectively. The uncertainty on all points is about the size of the symbol. The marks on the different column-density curves are ionization parameters separated by 0.2 dex. *Bottom panel*: same as top panel, for the nonvariable objects, with Seyfert 1 galaxies (*filled triangles*), Seyfert 2 galaxies (*open triangles*), and a BL Lac object (*open square*). The dotted straight lines give locii of power laws and broken power laws with different indices, as in Fig. 3. It can be seen that three objects, NGC 4151, NGC 3227, and NGC 3783, are significantly removed from the pure continuum tracks providing strong evidence for imprinted emission/absorption features.

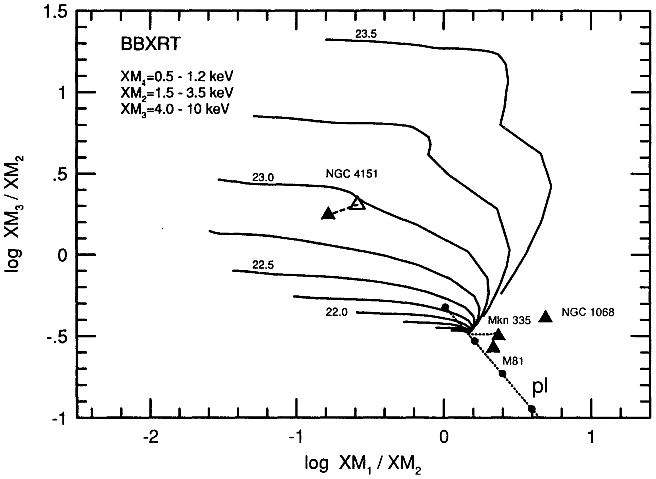

FIG. 7.—BBXRT color-color diagram for unabsorbed power laws of photon index 1.9 and full (emission and reflection included) models. The curves are marked with values of column density and the tick marks on the power-law ("pl") line are at $\Delta\Gamma = 0.5$. The two locations of the NGC 4151 observations are connected by a line. The filled triangle indicates the brighter phase, on day 5, and the open triangle the fainter phase, on day 6. The uncertainties are of the order of the symbol size.

observation. For objects with known color variations, we have separated each long observation into two locations, measured at time of "bright continuum" (*filled symbols*) and at times of "faint continuum" (*open symbols*; see Fig. 5 for those times). A line is drawn between the two to indicate the full range of colors. Objects in the bottom panel are separated into classes, Seyfert 1 galaxies, Seyfert 2 galaxies, and BL Lacs. Of all those, most object locations are consistent with a simple power-law continuum (see the dashed line passing through the bare-continuum point) and only three, NGC 4151, NGC 3227, and NGC 3783, are signficantly removed from it. All three galaxies in the top panel are significantly removed from that point during some phases. Thus we have six objects suspected for absorption. It is interesting to note that all the above six Seyfert galaxies are suspected of having absorbed X-ray spectrum, from previous studies (NGC 4151, Weaver et al. 1994; NGC 3783, Turner et al. 1993c; NGC 3227, George, Nandra, & Fabian 1990; Mrk 766, unpublished *EXOSAT* data; Mrk 335, Turner et al. 1993a). Thus, our color-color diagram provides a useful tool for identifying absorbed objects, especially for new *ROSAT* serendipitous sources, for which little information is available.

3.2. *The BBXRT Sample*

Several published observations of BBXRT are now available, and we show thsoe for four objects: the low-ionization nuclear emission-line region (LINER) M81 (Petre et al. 1993), the two Seyfert 1 galaxies NGC 4151 (Weaver et al. 1994) and Mark 335 (Turner et al. 1993a), and the Seyfert 2 galaxy NGC 1068 (Marshall et al. 1993). All observations were constrained to have Earth angle greater than 90°. The effective exposure times were 2734 s for M81, 2081 s for Mrk 335, and 2975 s for NGC 1068. As for NGC 4151, the object was observed twice, on mission days 5 and 6, with integration times of 1150 s and 1555 s, respectively. The data were selected to have been collected outside times when the instrument passed through the South Atlantic Anomaly, and to be free of contamination by solar X-rays (Sun angle ~114°).

The object locations on the BBXRT color-color diagram of XM_3/XM_2 versus XM_1/XM_2 were obtained by integrating the observed, Galactic-absorption–corrected counts over the specified bands. They are shown in Figure 7. It can be seen that three of the objects lie to the right of the bare-continuum point, while NGC 4151 exhibits significant spectral variability and is consistent with a warm absorber model.

4. DISCUSSION

We have shown how X-ray color-color diagrams can be used to analyze the physical properties of AGNs, in particular of the absorbed X-ray sources. As explained, the various bands and colors are easy to extract from the direct measurements. All that is required is to apply vignetting and Galactic-absorption corrections and to integrate the counts over the specified ranges (Table 1). The object location on the diagram is then investigated by comparison with a grid of theoretical models given here for a large range of conditions. Some zero

© American Astronomical Society • Provided by the NASA Astrophysics Data System

offset may be required, depending on the slope of the unabsorbed power-law continuum. This can easily be obtained from Figures 2, 3, and 7 by moving the bare-continuum point along the given power-law curves. Below is a brief discussion of the results derived from the *ROSAT* and BBXRT data sets we have presented, which illustrate several aspects of the method.

4.1. *Color-Color Analysis of ROSAT Data*

Many of the objects in our *ROSAT* sample fall close to the no-absorption locii (the power-law curve) on Figure 6, indicating that these AGNs are unlikely to contain the absorption or emission features expected in warm-absorber AGNs. These sources are not discussed further. The six Seyfert 1 galaxies that we found to be removed from the power-law curve deserve more attention.

Three Seyfert 1 galaxies (Fig. 6, *top panel*) show clear signs of X-ray color changes during continuum variations, and the motion in the color-color plane gives new physical insight about their properties. In all cases, there is an increase in XL_1/XL_2 during a decrease in X-ray luminosity. In two out of three cases (Mrk 335 and Mrk 766) XL_3/XL_2 decreases with decreasing continuum luminosity, and the third case (NGC 4051) shows the opposite behavior. This information in itself is a big improvement over the traditional hardness-ratio analysis (the equivalent of the XL_2/XL_1 ratio) that lacks the additional information provided by the additional dimension.

There are two possible interpretations of the change of location of Mrk 335 and Mrk 766 in the color-color plane. The first is a flattening of a power-law (or a broken power-law) continuum during bright continuum phases. Given the uncertainty in the measured colors, it can be seen from Figure 6 that for both objects the movement on the color-color plane is in the right direction (parallel to the "pl" line) and corresponds to a change in photon index of ~ 0.3. The second is an increase in the ionization parameter during continuum brightening, causing an increase in the level of ionization and a corresponding decrease in the amount of absorption. This explanation requires a very large column density absorber ($\sim 10^{23}$ cm^{-2}) and a large increase in ionization parameter compared with the observed variation (the uncertainties in the measured colors are consistent with this interpretation). We suspect that the first explanation is more appropriate. In the case of NGC 4051, the opposite behavior of XL_3/XL_2, combined with the location and movement on the color-color plane, suggests a real change in absorption properties for a small ($\sim 10^{21.5}$ cm^{-2}) column density absorber.

Three other Seyfert 1 galaxies (NGC 4151, NGC 3227, and NGC 3783), while not observed to be variable in the relatively short observations reported here, do occupy regions of the color-color plane associated with absorption. For all of these sources, the presence of absorption/emission features has already been suggested by spectral analysis (NGC 4151, Weaver et al. 1994; NGC 3783, Turner et al. 1993c; NGC 3227, the PSPC spectral data presented here). However, we note that the column density for NGC 4151 deduced here is much smaller than that obtained from other analysis, which we suspect is because we are unable to deconvolve the influence of the extended soft excess component from the absorber spectrum.

The caveat in the interpretation of *ROSAT* data is the correction due to neutral hydrogen absorption. A small uncertainty in the derived neutral column introduces a relatively large change in XL_1/XL_2 (see eq. [1]) and a large move in the color-color diagram. Given the uncertainty in the Galactic neutral column and the additional unknown absorbing neutral column in the source itself, we find this to be the main limitation of the method.

4.2. *Color-Color Analysis of BBXRT Data*

Out of the four objects in our BBXRT sample, three have been observed only once and for a short exposure time, thus no variability information is available.

The LINER M81 has been discussed by Petre et al. (1993) with the conclusion that the 0.5–10 keV continuum is consistent with an unabsorbed power law of photon slope 2.2. Our color analysis gives the same conclusion within the observational uncertainties. Mrk 335 has been discussed in Turner et al. 1993a (we note in passing that Turner et al. used a slightly shorter subset of the BBXRT data than we use here, as the daytime data were entirely excluded in their analysis). Turner et al. showed evidence for variability in absorption over the history of X-ray observations of the source, uncorrelated with flux changes in the continuum source. They showed no evidence for significant absorption in the BBXRT observation of Mrk 335, consistent with the location of Mrk 335 on the unabsorbed broken power-law line in Figure 7. The third case, the Seyfert 2 galaxy NGC 1068, has been discused in detail by Marshall et al. (1993). The signal in this source is large enough to show clear change in continuum slope, at about 3 keV. The continuum at higher energies, is very hard (photon slope of about 1.5), while the one below 3 keV is steep, with $\Gamma \simeq 3.4$. The location on the color-color diagram is consistent with such a spectrum.

The case of NGC 4151 is of the greatest importance since, as discussed by Weaver et al. (1994), the brightness of the source changed significantly during the BBXRT observations. The count rate during the day 5 BBXRT observations is about 1.7 times higher than during the day 6 observation, obtained some 18 hr later. This source is known to have a large absorption-like feature that has been interpreted as either due to partial covering or due to a warm absorber. Weaver et al. (1994) discussed all those possibilities and were able to show that, while a warm absorber model gives a satisfactory fit to the data on both days, it is inconsistent with the observed variability. They suggest that the reason is that the expected change is a decrease in ionization parameter from day 5 to day 6, but the best-fit warm absorber models indicate an opposite change. X-ray color analysis gives exactly the same conclusion without resorting to model fitting. The object location in Figure 7 changes opposite to the prediction of the warm absorber model (that should take the object from right to left as it goes from day 5 to day 6). We are thus led to the conclusion that the observed change in the strength of the X-ray absorption feature is a result of a large change in the hard (4–10 keV) and intermediate (1.5–3.5 keV) continua and almost no change in the soft 0.5–1.2 keV component. There is no variation on the XM_3/XM_2 ratio, within the uncertainties (see Weaver et al., Fig. 7), so much of the 1.5–3.5 keV flux is contributed by the variable hard component. We can rule out variations in the XM_3 band only, and we suspect a complicated situation involving variations in both continuum flux and absorption properties. Further discussion of NGC 4151 is beyond the scope of this paper; however, the source does demonstrate the success of the color-color technique in revealing such a behavior.

© American Astronomical Society • Provided by the NASA Astrophysics Data System

5. CONCLUSIONS

The new method of analyzing X-ray spectra presented in this paper has an advantage over several other methods. It is general, simple to apply, and enables spectral analysis with poor- or moderate-S/N data. Its use for the analysis of *ROSAT* data is limited by the uncertainties in Galactic absorption corrections but is superior to other methods in analyzing absorbed X-ray spectra. The method is more powerful when applied to *ASCA* and BBXRT data, which are not so sensitive to galactic columns. It enables a rough estimate of the column density and ionization parameter of absorbed sources, without resorting to models that are not available to all. The special case of variable-shape continuum can be investigated with conclusions about the reality of the absorption features. We find this analysis superior to the hardness-ratio method used in other papers.

H. N. acknowledges support by the US-Israel Binational Science Foundation (BSF grant 8900179) and NASA (grant NAG5-1813), and thanks the NRC for a senior research fellowship. T. J. T. and I. M. G. acknowledge the financial support of the Universities Space Research Association. We acknowledge useful discussions with many of our colleagues in the Laboratory for High Energy Astrophysics, in particular T. Kallman, G. Madejski, F. Marshall, R. Petre, and K. Weaver. This research has made use of data obtained through the High Energy Astrophysics Science Archive Research Center Online Service, provided by the NASA/Goddard Space Flight Center.

REFERENCES

Elvis, M., Fiore, F., Wilks, B., & McDowell, J. 1994, ApJ, 422, 60
George, I. M., Nandra, K., & Fabian, A. C. 1990, MNRAS, 242, 28p
Halpern, J. P. 1984, ApJ, 281, 90
Hasinger, G., Turner, T. J., George, I. M., & Boese, G. 1992, OGIP Calibration Memo CAL/ROS/92-001
Hasinger, G., Boese, G., Predehl, P., Turner, T. J., Yusaf, R., George, I. M., & Rohrbach, G. 1993, OGIP Calibration Memo CAL/ROS/93-015
Holt, S. S., Mushotzky, R. F., Becker, R. M., Bolt, E. A., Szymkowiak, A. E., & White, N. E. 1980, ApJ, 241, L13
Krolik, J. H., & Kallman, T. R. 1984, ApJ, 286, 366
Laor, A., Fiore, F., Elvis, M., Wilks, B. J., & McDowel, J. C. 1994, ApJ, in press
Liedhal, D. A., Kahn, S. M., Osterheld, A. L., & Goldstein, W. H. 1990, ApJ, 350, 137
Lightman, A. P., & White, T. R. 1988, ApJ, 335, 57
Marshall, F. E., et al. 1993, ApJ, 405, 168
Netzer, H. 1990, in Active Galactic Nuclei, ed. T. J.-L. Courvoisier & M. Mayer (Berlin and New York: Springer), 57
———. 1993, ApJ, 411, 594
Petre, R., Mushotzky, R. F., Serlemitsos, P., Jahoda, K., & Marshall, F. E. 1993, ApJ, 418, 644
Pfeffermann, E., et al. 1986, Proc. SPIE, 733, 519
Pounds, K., Nandra, K., Fink, H. H., & Makino, F. 1994, MNRAS, 267, 193p
Raymond, J. C. 1994, ApJ, in press
Raymond, J. C., & Smith, B. W. 1977, ApJ, 35, 419
Reichert, G. A., Mushotzky, R. F., & Holt, S. S. 1986, ApJ, 303, 87
Reichert, G. A., Mushotzky, R. F., Petre, R., & Holt, S. S. 1985, ApJ, 296, 69
Serlemitos, P., et al. 1992, in Frontiers of X-ray Astronomy, ed. Y. Tanaka & K. Koyama (Tokyo-Universal Academy), 221
Trümper, J. 1983, Adv. Space. Res., 2, 241
Turner, T. J., et al. 1993a, ApJ, 407, 556
Turner, T. J., George, I. M., & Mushotzky, R. F. 1993b, ApJ, 412, 72
Turner, T. J., Nandra, K., George, I. M., Fabian, A. C., & Pounds, K. A. 1993c, ApJ, 419, 127
Turner, T. J., Urry, C. M., & Mushotzky, R. F. 1993d, ApJ, 418, 653
Turner, T. J., Weaver, K. A., Mushotzky, R. F., Holt, S. S., & Madejski, G. M. 1991, ApJ, 381, 85
Walter, R., & Fink, H. H. 1993, A&A, 274, 105
Weaver, K. A., et al. 1994, ApJ, 423, 621
Wilkes, B. J., Elvis, M., Fiore, F., McDowell, J., Tananbaum, H., & Lawrence, A. 1992, ApJ, 393, L1
Yaqoob, T., Warwick, R. S., & Pounds, K. A. 1989, MNRAS, 236, 153